Editors' Suggestion | Featured in Physics

How Charges Separate when Surfaces Are Dewetted

Aaron D. Ratschow,[1] Lisa S. Bauer,[1] Pravash Bista,[2] Stefan A. L. Weber,[2,3,4] Hans-Jürgen Butt,[2] and Steffen Hardt[1,*]

[1]Institute for Nano- and Microfluidics, TU Darmstadt, Peter-Grünberg-Straße 10, D-64287 Darmstadt, Germany
[2]Max Planck Institute for Polymer Research, Ackermannweg 10, 55128 Mainz, Germany
[3]Department of Physics, Johannes Gutenberg University, Staudingerweg 10, 55128 Mainz, Germany
[4]Institute for Photovoltaics, University of Stuttgart, Pfaffenwaldring 47, 70569 Stuttgart, Germany

(Received 19 July 2023; revised 12 September 2023; accepted 9 April 2024; published 31 May 2024)

Charge separation behind moving water drops occurs in nature and technology. Yet, the physical mechanism has remained obscure, as charge deposition is energetically unfavorable. Here, we analyze how a part of the electric double layer charge remains on the dewetted surface. At the contact line, the chemical equilibrium of bound surface charge and diffuse charge in the liquid is influenced by the contact angle and fluid flow. We summarize the mechanism in an analytical model that compares well with experiments and simulations. It correctly predicts that charge separation increases with increasing contact angle and decreases with increasing velocity.

DOI: 10.1103/PhysRevLett.132.224002

Liquid drops interacting with solid surfaces play a role in many natural and technological processes. In nature, organisms have developed surfaces from which drops easily roll off to prevent fouling [1] or surfaces for fog harvesting [2]. Technological applications relying on the interaction between drops and surfaces include ink jet printing [3], condensation heat transfer [4,5], open droplet microfluidics [6,7], and application of spray droplets to plant leaves [8]. Already decades ago, it was noticed that water drops sliding along a hydrophobic, insulating surface acquire a charge [9]. However, only recently has this phenomenon moved into the focus of intense research [10–20], primarily driven by the intention to harvest electric energy [11,14–16,21,22]. Slide electrification can be either desired or undesired. In semiconductor manufacturing, wafers get damaged by electrostatic discharges that occur when rinsing them with aqueous solutions [23–25]. Slide electrification also occurs in nature when a water drop hits a plant leaf [26] but is suppressed by conductive substrates [27]. Recently, experiments with drops sliding along different surfaces have demonstrated the substantial influence that charging has on the motion of drops [27] and the possibility to manipulate drops electrostatically [18]. Moreover, the effect of slide electrification on contact angle hysteresis was uncovered [28]. Thus, drop charging is of fundamental importance in many dynamic wetting scenarios and profoundly influences drop trajectories along solid surfaces.

In spite of the widespread importance of drop charging, the underlying physical mechanisms of charge separation between the liquid and the solid surface have remained obscure, especially as it is energetically highly unfavorable to transfer a charge from the solid-water to the solid-air interface [17]. It is commonly assumed that a part of the surface charges forming the electric double layer (EDL) in water remains on the surface. However, this hypothesis alone does not provide any testable scientific framework. For example, it does not explain why slide electrification has been observed only on hydrophobic but not on hydrophilic surfaces [17,27], even though both form EDLs. A predictive theory would vastly advance the understanding of slide electrification and its implications. Models that account for the surface chemistry but neglect all processes at the three-phase contact line (CL) have been proposed and retrospectively fitted to experimental data with multiple free parameters [29,30]. Recently, a charge separation mechanism based on additional electron transfer was suggested [19,31]. Yet, no theory has been elaborated which takes into account the fundamental physical mechanisms and makes quantitative predictions. In the present Letter, we present a predictive theory that explains the charge separation mechanism based on transport processes in the vicinity of a receding CL. Our theoretical predictions agree well with experimental results.

Factors influencing charge separation.—A prerequisite for charge separation in aqueous drops is the EDL that forms on an initially uncharged solid surface when brought into contact with a liquid electrolyte like water. The EDL comprises bound surface charges and a diffuse layer of countercharges in the liquid with a characteristic thickness of $\lambda \approx 1$–1000 nm, called Debye length. Charge separation encompasses two essential steps. First, the surface acquires its bound net charge, screened by the diffuse layer. Second, the macroscopically electroneutral EDL separates at the receding CL, and a net charge remains on the dewetted surface, while the countercharge accumulates in the liquid

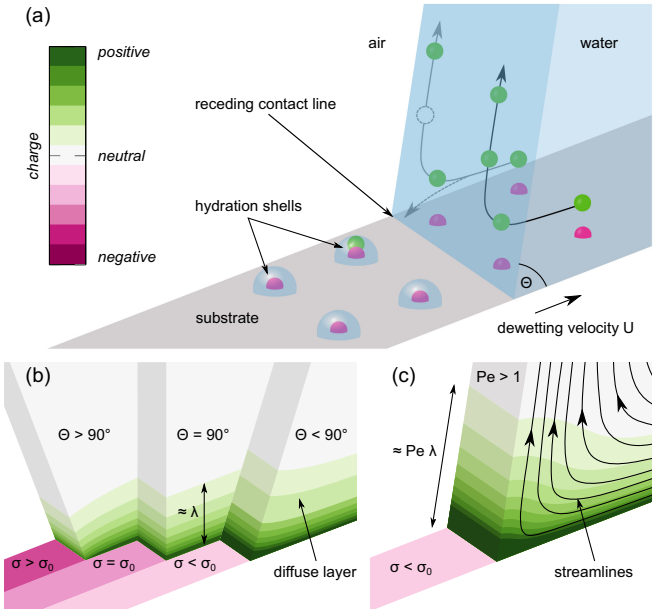

FIG. 1. Schematic representation of charge separation. All panels show a receding liquid wedge at the CL. Green and pink represent negative and positive charges, respectively. (a) Essential charge separation mechanism. Bound surface charges transfer from the wetted to the dewetted region as the CL recedes. These charges are surrounded by hydration shells, some of which contain a countercharge and, thus, neutralize it. (b) Contact angle effect. The EDL structure close to the CL is drawn for contact angles θ smaller than, equal to, and greater than $\pi/2$ for low dewetting velocities. The isopotential surfaces in the diffuse layer (characterized by the Debye length λ) warp due to the presence of the gas-liquid interface, which yields increasing surface charge densities σ for increasing contact angles (neglecting effects on the atomistic scale). (c) Flow effect for high dewetting velocities and, thus, Péclet numbers greater than one. Advective transport along the streamlines parallel to the gas-liquid interface expands the diffuse layer. (b) and (c) are obtained from simulations.

[Fig. 1(a)]. Surface chemistry, contact angle, and fluid flow determine the EDL structure at the CL and, thus, influence charge separation.

Surface chemistry.—Several processes can lead to a charged surface [32]. For a number of surfaces (like SiO_2), they can schematically be described by the reactions (Supplemental Material [33] Sec. 1.3) [34–36]

$$R-\mathrm{OH} \overset{K_A}{\longleftrightarrow} R-\mathrm{O}^- + \mathrm{H}^+, \tag{1}$$

$$\mathrm{H}^+ + R-\mathrm{OH} \overset{K_B}{\longleftrightarrow} R-\mathrm{OH}_2^+, \tag{2}$$

with the active surface sites $R-\mathrm{OH}$. Diffuse charges inside the liquid screen the surface charge, often quantified by the zeta potential ζ [37], which is the electrostatic potential drop across the diffuse layer in equilibrium and far from the CL (Appendix B). The surface chemistry yields a pH-dependent surface charge, specifically a point of zero charge (pzc), where the charge density vanishes [38]. The constants K_A and K_B determine ζ and the pzc. When the diffuse layer is disturbed near the CL, assuming an effective thickness $\lambda_{\mathrm{eff}} \neq \lambda$, the chemical equilibrium can shift and the potential across the diffuse layer (denoted as ϕ) can locally deviate from ζ. For $p\mathrm{H} > \mathrm{pzc}$, deprotonation [Eq. (1)] governs the potential ϕ [39]. The surface charge σ is then negative, and its equilibrium value as a function of the local proton concentration n_+ is (e, elementary charge; Γ, active site density)

$$\sigma = -\frac{e\Gamma}{1 + n_+/K_A}. \tag{3}$$

The surface charge obeys Gauss' law at the interface (ε, liquid permittivity; $\mathbf{n}$, surface normal vector; $\mathbf{E}$, electric field) [40]:

$$\sigma = -\mathbf{n}\cdot(\varepsilon\mathbf{E}) \approx \varepsilon\phi/\lambda_{\mathrm{eff}}. \tag{4}$$

We express the proton concentration with a Boltzmann factor $n_+ = n_0 \exp(\phi/\phi_T)$ ($\phi_T = kT/e \simeq 25$ mV, thermal potential; k, Boltzmann constant; T, temperature). Then, we apply the Debye-Hückel linearization, assuming $\phi/\phi_T < 1$, and eliminate σ from Eqs. (3) and (4) to obtain the potential drop across the diffuse layer due to deprotonation (Appendix B):

$$\phi = -\phi_T \frac{C\lambda_{\mathrm{eff}}/\lambda}{1 + K^{-1}(1 - \phi/\phi_T)}, \tag{5}$$

with the nondimensional constant $C = e\Gamma\lambda/(\varepsilon\phi_T)$ for the active site density Γ [41,42]. The nondimensional equilibrium constant $K = K_A/n_0$ can be inferred from the condition that, far from the CL, ϕ is equal to the zeta potential, $\phi|_{\lambda_{\mathrm{eff}}=\lambda} = \zeta$, yielding $K = (\zeta/\phi_T - 1)/(C\phi_T/\zeta + 1)$. The surface charge far from the CL, $\sigma_0 = \varepsilon\zeta/\lambda$, quantifies the charge that can potentially be separated in the dewetting process. Closer to the CL, however, contact angle, flow, and hydration effects alter the surface charge (Fig. 1). We assume that these effects are largely independent of each other and can be understood separately.

Contact angle effects.—We conceive the liquid shape at the CL as a wedge [43]. Figure 1(b) shows the EDL structure in the liquid close to the CL, obtained from detailed simulations of the Poisson-Nernst-Planck (PNP) and Stokes (S) equations in a wedge-shaped geometry at negligible velocities (Supplemental Material Sec. 1 [33]). For a contact angle $\theta = \pi/2$, the isopotential surfaces are planar and the EDL structure is the same everywhere in the liquid. However, for contact angles significantly deviating from $\pi/2$, the isopotential surfaces are significantly warped due to the presence of the gas-liquid interface, where we have $\mathbf{n}\cdot\mathbf{E} \approx 0$ due to Gauss' law and the high relative permittivity of water $\varepsilon_w \gg 1$.

In liquids, the diffuse layer screens the surface charge and establishes electroneutrality. Far from the CL, the diffuse countercharge distributes in the wall-normal direction. Yet, close to the CL, the countercharge distribution does not depend on only the wall-normal coordinate. For $\theta > \pi/2$, the countercharge distributes over a larger, and for $\theta < \pi/2$ over a smaller, angular domain. Because larger (smaller) angular domains can accommodate more (less) countercharge, the local surface charge at the CL increases for $\theta > \pi/2$ and decreases for $\theta < \pi/2$. Dörr and Hardt [44] quantitatively analyzed the contact-angle influence on the EDL structure and derived the ratio of nondimensional potential drop across the diffuse layer and surface charge density, $g(\theta) = \pi/(2\theta)$, for angles around $\pi/2$ and no flow. Assuming an approximately constant potential drop $\phi = \zeta$ (Supplemental Material Sec. 2.2 [33]), the surface charge density in the liquid at the CL is

$$\sigma_{\mathrm{CL}}(\theta) = \frac{\varepsilon\phi}{\lambda_{\mathrm{eff}} g(\theta)}. \tag{6}$$

This purely geometrical effect is present even at negligible velocities.

Flow effects.—Since liquid adheres to the solid surface, CL movement induces a flow in the liquid [43]. The streamlines follow the solid-liquid and gas-liquid interfaces, switching directions close to the CL [Fig. 1(c)]. Thus, close to the CL, the wall-normal flow advects ions in the EDL against the electrostatic attraction of the surface charge and modifies the diffuse layer.

To characterize this advective influence, we introduce the Péclet number that measures the importance of advective over diffusive transport. It is defined as $\mathrm{Pe} = U\lambda/D$, with the Debye length λ as the only local length scale, ion diffusivity $D \approx 1 \times 10^{-9}$ m^2/s [45,46], and dewetting velocity U. For reference, at $U = 10$ cm/s and $\lambda = 10$ nm, we obtain $\mathrm{Pe} \approx 1$. Because of mass conservation, the velocity directly along the gas-liquid interface is essentially U [Fig. 1(c)] and points in the wall-normal direction for contact angles $\theta \simeq \pi/2$. Under the Debye-Hückel approximation, the conductivity $\kappa = D(n_+ + n_-)e^2/(kT)$ (for monovalent symmetric electrolytes) is approximately constant with a value of $\kappa = D\varepsilon\lambda_D^{-2}$, and the space-charge density in the diffuse layer ρ_v obeys [47]

$$\nabla \cdot (\rho_v \mathbf{u}) = D\nabla^2\rho_v - \frac{\kappa}{\varepsilon}\rho_v. \tag{7}$$

When considering a one-dimensional version of this equation in the wall-normal direction with $\mathbf{u} = U\mathbf{n}$, an analytical solution can be computed that exhibits an exponential decay of the space-charge density and the electrostatic potential over an effective length λ_{eff} (Appendix B):

$$\lambda_{\mathrm{eff}} = \frac{\sqrt{\mathrm{Pe}^2 + 4} + \mathrm{Pe}}{2}\lambda. \tag{8}$$

For $\mathrm{Pe} \ll 1$, diffusion and electromigration balance, and the diffuse layer has a characteristic thickness of $\lambda_{\mathrm{eff}}(\mathrm{Pe} \ll 1) \simeq \lambda$. In the regime of $\mathrm{Pe} > 1$, diffusion is of minor importance, and electromigration is mainly balanced by advection. The flow expands the diffuse layer close to the CL to a thickness $\lambda_{\mathrm{eff}}(\mathrm{Pe} > 1) \simeq \mathrm{Pe}\lambda$ [Fig. 1(c)].

Theoretical model for the surface charge at the contact line.—The EDL structure depends on the contact angle and the flow expanding the diffuse layer. Building on this, we formulate a model for the electrostatic potential and surface charge density at the CL. We combine the surface chemistry equation (5), Eq. (6) for the surface charge density, and the advectively expanded Debye length [Eq. (8)] and solve for ϕ to obtain (Appendix B)

$$\frac{\phi_{\mathrm{CL}}(\mathrm{Pe})}{\phi_T} = \frac{1}{2}(K+1) - \sqrt{\frac{1}{4}(K+1)^2 + KC\lambda_{\mathrm{eff}}/\lambda},$$
$$\sigma_{\mathrm{CL}}(\theta, \mathrm{Pe}) = \frac{\varepsilon\phi_{\mathrm{CL}}}{\lambda_{\mathrm{eff}} g(\theta)}. \tag{9}$$

The surface charge density in the liquid far from the CL is $\sigma_0 = \sigma_{\mathrm{CL}}(\theta = \pi/2, \mathrm{Pe} = 0)$, because the wall-normal flow there is zero. As the CL approaches, it gradually changes from σ_0 to σ_{CL} (Supplemental Material Sec. 1.7 [33]). At the CL, the surface charge is dewetted.

Effects on the atomistic scale.—The model of Eq. (9) describes the influence of the EDL structure at the CL on charge separation using continuum theory. Comparing the predictions of our model and the numerical simulations to experiments indicates that the magnitude of the deposited surface charge is somewhat smaller than predicted, by a factor ω in the range 0.1–1. We attribute this to effects on the atomistic scale, beyond the validity of continuum theory. We hypothesize that dewetted, surface-bound charges retain a thin hydration shell of water molecules [Fig. 1(a)] (Supplemental Material Sec. 2.4 [33]), probably from the dewetting liquid with a high counterion concentration [17]. When some counterions transfer to the hydration shells, the apparent net surface charge diminishes. A value of $\omega = 0.5$ would mean that half of the dewetted surface charge is neutralized by counterions in hydration shells [Fig. 1(a)]. This effect likely depends on the ion type and solid surface composition, among others. A quantification would require complex molecular dynamics simulations and is beyond the scope of this study. To account for the effects on the atomistic scale, we assume that σ_{CL} is diminished by a constant factor of $\omega \leq 1$. We hypothesize that EDL effects and atomistic effects during charge separation are largely independent. Thus, our model should be able to predict experimental trends.

Predictions and implications.—When comparing surfaces with equal zeta potentials, theory predicts that charge separation is highest on hydrophobic surfaces [Figs. 2(a) and 2(b)], since the scaled surface charge $\sigma_{\mathrm{CL}}/\sigma_0$ increases with increasing receding contact angle. According to the

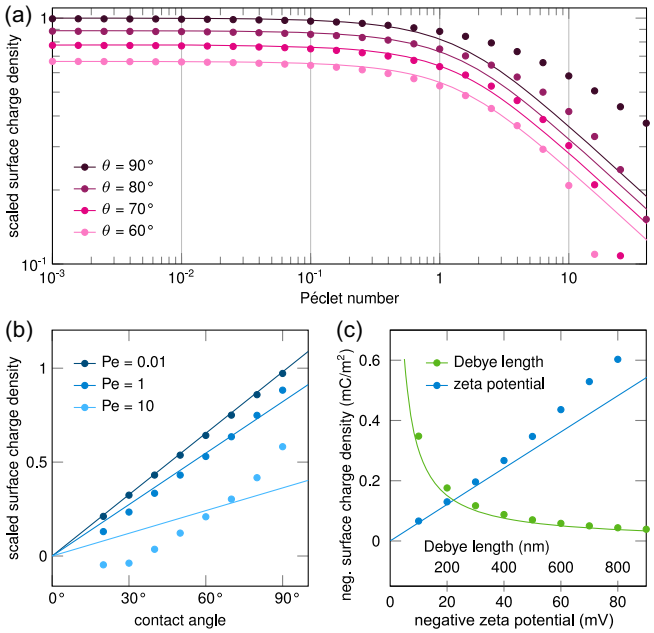

FIG. 2. Parametric dependencies of the surface charge density at the CL on the liquid side. The graphs compare analytical (lines) with numerical results (symbols). All calculations use a Debye length of $\lambda = 100$ nm and a zeta potential of $\zeta = -50$ mV, if not stated otherwise. The Péclet number Pe is varied via the dewetting velocity U. Assuming a constant influence of effects on the atomistic scale ($\omega = \text{const}$), the scaled surface charge density is a direct measure for charge separation. (a) Scaled surface charge density σ_{CL}/σ_0 at the CL as a function of the Péclet number at different contact angles θ and (b) as a function of the receding angle at different Péclet numbers. (c) Negative value of the surface charge density at the CL $-\sigma_{CL}$ as a function of the Debye length λ (green) and the negative zeta potential (blue) at $\text{Pe} = 0.01$ and $\theta = 80°$.

theory, there should be two distinct Péclet number regimes [Fig. 2(a)]. Up to $\text{Pe} \simeq 1$, charge separation is little affected by the flow. From $\text{Pe} \simeq 1$ on, advection reduces charge separation with increasing velocity, which is somewhat counterintuitive when comparing this dependency to observations in flow electrification [48,49] or solid-solid contact electrification [50]. The decreasing charge separation is caused by the expansion of the diffuse layer, which reduces the surface charge.

Note that the presented model neglects electric fields in the substrate, corresponding to a grounded liquid [compare Fig. 3(a)]. A more general model is derived in Appendix B.

Numerical validation.—The analytical model incorporates some simplifying assumptions (Supplemental Material Sec. 2.1 [33]). We assess these by comparing the model predictions to detailed finite-element simulations of the full PNP-S equations, incorporating the full flow field with Navier slip at the solid-liquid interface (slip length $l_s = 1$ nm) as well as charge regulation via the reactions of Eqs. (1) and (2), solved in a 2D wedge geometry. We ensure grid independence and negligible finite-size effects (Supplemental Material Sec. 1 [33,51–53]). Figure 2(a) shows excellent agreement for the scaled surface charge σ_{CL}/σ_0 up to $\text{Pe} \simeq 1$ and for contact angles $< 90°$ up to $\text{Pe} \simeq 10$. At higher Péclet numbers and contact angles, the contact angle and flow effects are no longer independent, as assumed in the analytical model. Although the expression for the contact angle influence $g(\theta)$ is linearized around $\theta = 90°$ [44,54], it holds well for angles down to 20° [Fig. 2(b)], again with deviations at higher Pe. For low contact angles and high Péclet numbers, the proton concentration and, thus, the local pH can exceed the pzc. Here, the surface charge polarity flips due to proton adsorption, not captured by the analytical model (Supplemental Material Sec. 1.8 [33]) [55]. The model fairly accurately captures the dependence on zeta potential and Debye length [Fig. 2(c)], even beyond the range of validity of the Debye-Hückel approximation, $\zeta < \phi_T \simeq 25$ mV.

Experimental validation.—To validate the proposed theory of charge separation, we compare our model, Eqs. (9), to experimental data. In the experiments (Appendix A), schematically shown in Fig. 3(a), 1 mM KNO_3 and NaCl aqueous drops slide down an uncharged hydrophobic glass substrate. We control the slide velocity via the inclination angle α and measure it optically via a laser diode and a light barrier. The drop slides along a tungsten wire grounded through a femtoampere meter. At initial contact, the drop discharges [Fig. 3(b), peak current]. While in contact, the grounded drop continuously deposits surface charge, measured by the tail current I_{tail}. In Fig. 3(c), we compare the deposited surface charge density $\sigma_{out} = I_{tail}/(Uw)$ (U, drop velocity; w, drop width) [40] to our model predictions. We use the Cox-Voinov model (CVM) [56,57] to account for the dynamic changes of the receding contact angle. Atomistic effects are represented by the fitting parameter ω. With $\omega_{NaCl} = 0.35$ and $\omega_{KNO_3} = 0.39$ and $\sigma_{out} = \omega\sigma_{CL}$, we obtain a fair agreement between theory and experiments for both salts up to $\text{Pe} \simeq 4$. Deviations for larger Péclet numbers are expected, since the CVM becomes inaccurate at non-negligible Reynolds numbers (Appendix B). The decreasing charge separation at higher velocities is immediately apparent in the experimental results.

Conclusions and outlook.—In conclusion, while the practical implications of slide electrification have been extensively explored, the lack of its understanding and a theory with predictive power has hindered their dissemination. We have developed and validated a theoretical model that describes the slide electrification at receding contact lines as the partial transfer of surface charges from the wet to the dry region. This means that slide electrification is a universal phenomenon that often occurs in the dynamic wetting of surfaces by electrolytes. The deposited charge increases with the zeta potential. Charge separation is strongest on hydrophobic substrates with high contact angles and—contrary to other contact electrification

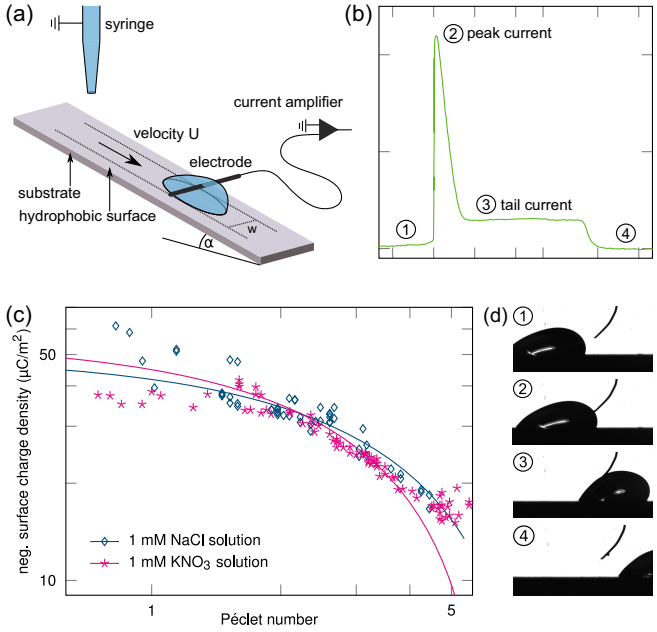

FIG. 3. Validation by means of experiments on slide electrification. (a) Schematic of the experimental setup. A drop slides down an inclined hydrophobic surface and accumulates a charge due to charge separation at the CL. When touching the electrode, the drop discharges and the arising current is recorded. (b) Typical profile of the measured current during the contact time between drop and electrode. The peak current arises due to the discharge of the drop charge accumulated over the slide path before contacting the electrode. The tail current measures the deposited charge during contact. (c) Comparison of analytical (line) and experimental results (dots) for different Péclet numbers ($\omega_{\mathrm{NaCl}} = 0.35$, $\omega_{\mathrm{KNO_3}} = 0.39$, $w = 5$ mm). (d) Photographs of a drop passing the electrode.

mechanisms—decreases with the dewetting velocity. Our analytical model quantitatively predicts these parametric trends, in agreement with numerical simulations and experiments. The relevant dependencies of charge separation on velocity and contact angle have been identified and can be probed in further experiments. We believe that our results provide new insights into findings that are hard to explain without considering charge separation, among others: printing processes, contact angle hysteresis, dewetting of films on surfaces, autophobing, frost formation on surfaces, cleaning of surfaces, and spraying of herbicides and pesticides. By lifting some of the simplifying assumptions, our theory could be extended in different directions and could, therefore, form the nucleus of a class of models for charge separation by dewetting.

We thank Maximilian T. Schür for helpful discussions on the simulations, Xiaomei Li for providing the experimental photographs, and Chirag Hinduja for preliminary measurements at low velocities. This work was supported by the German Research Foundation (DFG) within the Collaborative Research Centre 1194 "Interaction of Transport and Wetting Processes," Project ID No. 265191195, subproject A02b (S. H. and A. D. R.) and subproject C07 (H.-J. B.), the Department for Process and Plant Safety of Bayer AG, Leverkusen, Germany (A. D. R.), and the European Research Council (ERC) under the European Union's Horizon 2020 research and innovation program (Grant Agreement No. 883631) (P. B. and H.-J. B.).

S. H. and H.-J. B. proposed the work, A. D. R. developed the theoretical framework and the analytical model, L. S. B. carried out the simulations and proposed the measurement method, P. B. and S. A. L. W. conducted the experiments, A. D. R., L. S. B., S. H., and H.-J. B. contributed to the interpretation of the results, A. D. R., L. S. B., and S. H. prepared the manuscript, and S. H. and H.-J. B. supervised the work.

Appendix A: On experiments.—The hydrophobic samples consist of glass slides ($25 \times 70 \times 1$ mm) coated with trichloro(1H,1H,2H,2H-perfluorooctyl)silane (PFOTS) (Sigma-Aldrich Chemie GmbH) using chemical vapor deposition. Before coating, the substrates are cleaned with acetone and ethanol and treated in an oxygen plasma cleaner (Diener electronic, Femto BLS) for 10 min at 300 W to activate the surface. Then, the slides and a 1 ml vial of PFOTS are placed into a vacuum desiccator and evacuated to 100 mbar. The resulting hydrophobic surfaces have advancing and receding contact angles of $107 \pm 2°$ and $89 \pm 3°$, respectively, and a root-mean-square roughness of < 1 nm across 0.5×0.5 μm^2 [27]. All experiments are performed in an inert nitrogen atmosphere under ambient conditions (atmospheric pressure; temperature, 21 ± 1 °C; humidity, $50 \pm 2\%$). The hydrophobic sample is placed on a grounded metal plate inside the humidity chamber, and the surface is neutralized by an ionizing air blower (Mini Zero Volt Ionizer 2, ESD) for 5 min. After a waiting time of some minutes to equilibrate the ion concentration in the air, a peristaltic pump (Minipuls 3, Gilson) produces a 45 μL drop of 1 mM KNO_3 or NaCl solution ($p\mathrm{H} \approx 5.5$). After falling 0.5 ± 0.2 cm from the grounded syringe needle, the drop slides for 5.0 ± 0.2 cm where a measuring electrode discharges it. A transimpedance current amplifier (rise time 0.8 ms) (DDPCA-300, Femto), triggered by a light barrier (laser diode CPS186, Thorlabs) placed 1.0 ± 0.2 cm in front of this electrode, records the arising current through a data acquisition board (USB-6366 x-Series, NI). The discharge of accumulated drop charge causes a peak current. While in contact with the grounded wire, ongoing charge separation manifests as a tail current [Fig. 3(b)]. Assuming a constant surface charge σ_{out} across the drop width w, the total integrated current leaving the drop is equal to the increase of charge behind the drop on the dewetted area A, $I_{\mathrm{tail}} = \sigma_{\mathrm{out}} dA/dt = \sigma_{\mathrm{out}} U w$. The

velocity U is determined from the delay between the laser trigger and the onset of current and is adjusted by the inclination angle of the humidity chamber via a tilting stage. The measured velocities U are translated to corresponding Péclet numbers $\mathrm{Pe} = U\lambda/D$ with the Debye length $\lambda = \sqrt{\varepsilon RT/(2z^2 c_0 F^2)} = 9.7$ nm at $c_0 =$ 1 mM and the effective diffusivity of the salts [58] of $D = 2 \times 10^{-9}$ m^2/s and 1.6×10^{-9} m^2/s for KNO_3 and NaCl, respectively [28,45]. The zeta potential of the specific substrate used, $\zeta_0 = -35$ mV [59], is rescaled according to $\zeta = \zeta_0 \lambda/\lambda_0$ [60], where $\lambda_0 = 173$ nm is the Debye length of de-ionized water in equilibrium with atmospheric CO_2, $p\mathrm{H} = 5.5$ [59]. The active site density on the substrate is $\Gamma = 5$ nm^{-2} [41,42].

Appendix B: On theory.—The analytical model quantifies the bound surface charge at the receding CL. The version presented in this section also accounts for electric fields in the substrate of thickness d due to a nonzero potential difference V_l between the liquid and a grounded subsurface electrode, as caused by drop charge accumulation [40]. It simplifies to the model in the main text when the drop is uncharged.

Surface chemistry: We consider only deprotonation [Eq. (1)], which governs the surface chemistry for $p\mathrm{H} \gg \mathrm{pzc}$, and assume chemical equilibrium, justified by the small timescale of the reaction $\approx 1 \times 10^{-6}$ s [32]. The surface charge density then follows the law of mass action, Eq. (3). The local proton concentration in the liquid follows a Boltzmann distribution $n_{\mathrm{H}^+} = n_0 \exp(-\phi/\phi_T)$ with the potential drop across the diffuse layer ϕ and the bulk proton concentration n_0. We obtain

$$\sigma = -\frac{e\Gamma}{1 + K^{-1}\exp(\phi/\phi_T)}, \tag{B1}$$

where $K = K_A/n_0$. The surface charge density σ and the potential drop across the diffuse layer are coupled through surface chemistry [Eq. (B1)] and through electrostatics via Gauss' law at the solid-liquid interface $\mathbf{n} \cdot (\varepsilon_l \mathbf{E}_l - \varepsilon_s \mathbf{E}_s) = \sigma/\varepsilon_0$ (l, liquid; s, solid). Under the Debye-Hückel approximation $\phi < \phi_T$, the electric field in the liquid is $\mathbf{n} \cdot \mathbf{E}_l \approx \phi/\lambda$. For the electric field in the solid, we neglect the Stern layer capacitance, as it is much larger than both the dielectric and the diffuse layer capacitance [35], and account for the field between the liquid and a grounded subsurface electrode, $\mathbf{n} \cdot \mathbf{E}_s = -V_l/d$. Gauss' law yields [40]

$$\sigma = \frac{\varepsilon_0 \varepsilon_l \phi}{\lambda} + \frac{\varepsilon_0 \varepsilon_s V_l}{d}. \tag{B2}$$

Combining Eqs. (B1) and (B2), we get

$$\phi = \frac{C\phi_T}{1 + K^{-1}\exp(-\phi/\phi_T)} - V\phi_T, \tag{B3}$$

with the nondimensional groups $C = e\Gamma\lambda/(\varepsilon_0 \varepsilon_l \phi_T)$ for the active site density and $V = \varepsilon_s \lambda V_l/(\varepsilon_l d \phi_T)$ for the liquid potential. This implicit equation for ϕ cannot be solved analytically. We, thus, linearize the exponential function using the Debye-Hückel approximation and arrive at

$$\phi = \frac{C\phi_T}{1 + K^{-1}(1 - \phi/\phi_T)} - V\phi_T, \tag{B4}$$

which becomes Eq. (3) for $V_l = V = 0$.

Contact angle effect: Dörr and Hardt [44] derived an implicit analytical solution of the linearized Poisson-Boltzmann equation $\nabla^2\Psi = \lambda^{-2}\Psi$ near a CL with contact angle θ. The equipotential surfaces warp near the CL due to the presence of the gas-liquid interface [Fig. 1(b)], where the boundary condition is approximated by a zero normal electric field due to the high permittivity of water compared to air. For contact angles around $\theta = \pi/2$, they derived the generic relationship

$$\frac{\phi_{\mathrm{CL}}}{\phi}\frac{\sigma}{\sigma_{\mathrm{CL}}} = \frac{\pi}{2\theta} \coloneqq g(\theta), \tag{B5}$$

where the subscript CL denotes quantities at the CL and quantities without subscript are to be evaluated far from the CL. In our simulations at low Péclet numbers, we observe only minor changes in the potential across the diffuse layer when approaching the CL, $\phi_{\mathrm{CL}} \simeq \phi$ (Supplemental Material Sec. 2.3 [33]), and, thus, we use the approximation $\sigma_0/\sigma_{\mathrm{CL}} = g(\theta)$. Consequently, the surface charge at the CL becomes

$$\sigma_{\mathrm{CL}}(\theta) = \frac{\varepsilon_0 \varepsilon_l \zeta}{\lambda g(\theta)} + \frac{\varepsilon_0 \varepsilon_s V_l}{d}, \tag{B6}$$

which simplifies to Eq. (4) for $V_l = 0$. Note that an exact expression for $g(\theta)$, valid for arbitrary contact angles, was derived in [54].

Flow effect: Near the CL, wall-normal advective transport affects the charges in the diffuse layer. For symmetric electrolytes, the Nernst-Planck equations for ion transport can be transformed into equations for the space-charge density $\rho_v = e(n_+ - n_-)$ and the ionic conductivity $\kappa = eD(n_+ + n_-)/\phi_T$. In the Debye-Hückel limit, the conductivity is constant and the stationary space-charge density obeys Eq. (7) [47]. When the hydrodynamic slip length is small compared to the Debye length, mass conservation demands that the velocity along the solid-liquid and the velocity along the gas-liquid interface within the EDL are essentially the dewetting velocity U. Larger slip lengths $\approx\lambda$ slightly reduce advection within the EDL. We use Eq. (7) in wall-normal direction y and with the velocity $\mathbf{n} \cdot \mathbf{u} = U$ for the EDL at the CL:

$$D\frac{\partial^2 \rho_v}{\partial y^2} - U\frac{\partial \rho_v}{\partial y} - \frac{\kappa}{\varepsilon_0 \varepsilon_l}\rho_v = 0. \tag{B7}$$

We analytically solve it alongside the one-dimensional Poisson equation $\partial^2\psi/\partial y^2 = -\rho_v/(\varepsilon_0\varepsilon_l)$, with the boundary conditions $\rho_v = \rho_{v,0}$ and $\psi = \psi_0$ on the surface at the CL ($y = 0$) and $\partial\rho_v/\partial y = \partial\psi/\partial y = 0$ far from the surface ($y \to \infty$). This results in

$$\psi = \psi_0 \exp(-y/\lambda_{\mathrm{eff}}), \tag{B8}$$

$$\lambda_{\mathrm{eff}} = \lambda \frac{\sqrt{\mathrm{Pe}^2 + 4} + \mathrm{Pe}}{2}, \tag{B9}$$

with $\lambda = \sqrt{\varepsilon_0\varepsilon_l D/\kappa}$ and $\mathrm{Pe} = U\lambda/D$. Apparently, the diffuse layer structure is exponential, like in the case without wall-normal flow, but the characteristic thickness increases to λ_{eff}.

Full analytical model: To obtain the full analytical model, we solve the linearized equation (B4) with the effective Debye length from Eq. (B9) for the potential drop across the diffuse layer at the CL:

$$\phi_{\mathrm{CL}}(V_l, \mathrm{Pe}) = \frac{1}{2}(K - V + 1) - \sqrt{\frac{1}{4}\left(K - V\frac{\lambda_{\mathrm{eff}}}{\lambda} + 1\right)^2 + V\frac{\lambda_{\mathrm{eff}}}{\lambda}(K + 1) + KC\frac{\lambda_{\mathrm{eff}}}{\lambda}}. \tag{B10}$$

Finally, we use Eq. (B6) along with Eq. (B9) to find the surface charge density at the CL:

$$\sigma_{\mathrm{CL}}(V_l, \mathrm{Pe}, \theta) = \frac{\varepsilon_0\varepsilon_l\phi_{\mathrm{CL}}}{\lambda_{\mathrm{eff}} g(\theta)} + \frac{\varepsilon_0\varepsilon_s V_l}{d}. \tag{B11}$$

Equations (B10) and (B11) are the generalized forms of Eqs. (9) in the main text for arbitrary liquid potentials V_l.

Dynamic contact angle: The analytical model captures the parametric dependencies on the receding contact angle as well as on the dewetting velocity measured by the Péclet number and treats the two effects independently. In general, the dynamic receding contact angle is velocity dependent. To account for this dependency when comparing the model to experimental results [Fig. 3(c)], we use the Cox-Voinov model. It relates the dynamic receding contact angle θ to the static receding contact angle θ_r via $\theta^3 = \theta_r^3 + 9\mathrm{Ca}\ln(l_M/l_\mu)$, with the capillary number $\mathrm{Ca} = \eta U/\gamma$ (η, liquid viscosity; γ, liquid surface tension). The receding contact angle is $\theta_r = 89°$ for the PFOTS substrate used. The expression l_M/l_μ is the ratio of the macroscopic and microscopic length scales, where the microscopic length scale l_μ is related to the size of molecules $\approx$1 nm [56,57]. As per [57,61], the ratio is $l_M/l_\mu = 10^4$. The model is valid only for low Reynolds numbers < 1, expressed as $\mathrm{Re} = U l_M \rho/\eta$ (η/ρ, kinematic liquid viscosity). For our experimental conditions of $\lambda \approx 10$ nm, the Reynolds number is approximately twice the Péclet number, and, thus, the Cox-Voinov model loses validity for high $\mathrm{Re} \simeq 2\,\mathrm{Pe}$, as discussed in the text.

*hardt@nmf.tu-darmstadt.de

[1] W. Barthlott and C. Neinhuis, Planta **202**, 1 (1997).
[2] A. R. Parker and C. R. Lawrence, Nature (London) **414**, 33 (2001).
[3] D. Lohse, Annu. Rev. Fluid Mech. **54**, 349 (2022).
[4] X. Hu, Q. Yi, X. Kong, and J. Wang, Appl. Sci. **11**, 1553 (2021).
[5] T.-Y. Zhang, L.-W. Mou, M.-J. Liu, and L.-W. Fan, Int. J. Therm. Sci. **172**, 107309 (2022).
[6] M. G. Pollack, R. B. Fair, and A. D. Shenderov, Appl. Phys. Lett. **77**, 1725 (2000).
[7] S. K. Cho, H. Moon, and C.-J. Kim, J. Microelectromech. Syst. **12**, 70 (2003).
[8] N. M. Kovalchuk and M. J. Simmons, Curr. Opin. Colloid Interface Sci. **51**, 101375 (2021).
[9] K. Yatsuzuka, Y. Mizuno, and K. Asano, J. Electrost. **32**, 157 (1994).
[10] Z.-H. Lin, G. Cheng, S. Lee, K. C. Pradel, and Z. L. Wang, Adv. Mater. **26**, 4690 (2014).
[11] Y. Sun, X. Huang, and S. Soh, Chem. Sci. **6**, 3347 (2015).
[12] M. D. Boamah, E. H. Lozier, J. Kim, P. E. Ohno, C. E. Walker, T. F. Miller, and F. M. Geiger, Proc. Natl. Acad. Sci. U.S.A. **116**, 16210 (2019).
[13] B. He and A. A. Darhuber, J. Micromech. Microeng. **29**, 105002 (2019).
[14] W. Xu, H. Zheng, Y. Liu, X. Zhou, C. Zhang, Y. Song, X. Deng, M. Leung, Z. Yang, R. X. Xu, Z. L. Wang, X. C. Zeng, and Z. Wang, Nature (London) **578**, 392 (2020).
[15] H. Wu, N. Mendel, D. van den Ende, G. Zhou, and F. Mugele, Phys. Rev. Lett. **125**, 078301 (2020).
[16] A. Shahzad, K. R. Wijewardhana, and J.-K. Song, Appl. Phys. Lett. **113**, 023901 (2018).
[17] A. Z. Stetten, D. S. Golovko, S. A. L. Weber, and H.-J. Butt, Soft Matter **15**, 8667 (2019).
[18] Q. Sun, D. Wang, Y. Li, J. Zhang, S. Ye, J. Cui, L. Chen, Z. Wang, H.-J. Butt, D. Vollmer, and X. Deng, Nat. Mater. **18**, 936 (2019).
[19] S. Lin, L. Xu, A. Chi Wang, and Z. L. Wang, Nat. Commun. **11**, 399 (2020).
[20] D. Choi, H. Lee, D. J. Im, I. S. Kang, G. Lim, D. S. Kim, and K. H. Kang, Sci. Rep. **3**, 2037 (2013).
[21] L. E. Helseth, J. Electrost. **81**, 64 (2016).
[22] Y. Wang, S. Gao, W. Xu, and Z. Wang, Adv. Funct. Mater. **30**, 1908252 (2020).
[23] K. Dhane, J. Han, J. Yan, O. Mahdavi, D. Zamani, B. Vermeire, and F. Shadman, IEEE Trans. Semicond. Manuf. **24**, 125 (2011).

[24] K.-I. Sano, R. Dylewicz, X. Man, D. Mui, J. Zhu, and M. Kawaguchi, Solid State Phenom. **255**, 277 (2016).
[25] T. Guo, T. H. Tsai, C. C. Chien, M. Chan, C. L. Yang, and J. Y. Wu, Solid State Phenom. **187**, 63 (2012).
[26] S. Armiento, C. Filippeschi, F. Meder, and B. Mazzolai, Commun. Mater. **3**, 79 (2022).
[27] X. Li, P. Bista, A. Z. Stetten, H. Bonart, M. T. Schür, S. Hardt, F. Bodziony, H. Marschall, A. Saal, X. Deng, R. Berger, S. A. L. Weber, and H.-J. Butt, Nat. Phys. **18**, 713 (2022).
[28] X. Li, A. D. Ratschow, S. Hardt, and H.-J. Butt, Phys. Rev. Lett. **131**, 228201 (2023).
[29] R. Zimmermann, N. Rein, and C. Werner, Phys. Chem. Chem. Phys. **11**, 4360 (2009).
[30] M. D. Sosa, N. B. D'Accorso, M. L. Martínez Ricci, and R. M. Negri, Langmuir **38**, 8817 (2022).
[31] L. E. Helseth, Langmuir **39**, 1826 (2023).
[32] R. A. Jacobs and R. F. Probstein, AIChE J. **42**, 1685 (1996).
[33] See Supplemental Material at http://link.aps.org/supplemental/10.1103/PhysRevLett.132.224002 for details, parameters, and verification of the numerical simulations, and for underlying assumptions and their justification regarding the analytical model.
[34] D. E. Yates, S. Levine, and T. W. Healy, J. Chem. Soc., Faraday Trans. 1 **70**, 1807 (1974).
[35] E. J. van der Wouden, D. C. Hermes, J. G. E. Gardeniers, and A. van den Berg, Lab Chip **6**, 1300 (2006).
[36] J. M. Paz-Garcia, B. Johannesson, L. M. Ottosen, A. B. Ribeiro, and J. M. Rodriguez-Maroto, Electrochim. Acta **150**, 263 (2014).
[37] H.-J. Butt, K. Graf, and M. Kappl, *Physics and Chemistry of Interfaces*, 1st ed. (Wiley-VCH, Weinheim, 2006).
[38] T. Preočanin, A. Selmani, P. Lindqvist-Reis, F. Heberling, N. Kallay, and J. Lützenkirchen, Colloids Surf. A **412**, 120 (2012).
[39] S. H. Behrens and D. G. Grier, J. Chem. Phys. **115**, 6716 (2001).
[40] P. Bista, A. D. Ratschow, H.-J. Butt, and S. A. L. Weber, J. Phys. Chem. Lett. **14**, 11110 (2023).
[41] R. van Hal, J. Eijkel, and P. Bergveld, Adv. Colloid Interface Sci. **69**, 31 (1996).
[42] I. Christl and R. Kretzschmar, Geochim. Cosmochim. Acta **63**, 2929 (1999).
[43] C. Huh and L. Scriven, J. Colloid Interface Sci. **35**, 85 (1971).
[44] A. Dörr and S. Hardt, Phys. Rev. E **86**, 022601 (2012).
[45] V. Daniel and J. G. Albright, J. Solution Chem. **20**, 633 (1991).
[46] P. W. Atkins, J. de Paula, and J. J. Keeler, *Atkins' Physical Chemistry*, 11th ed. (Oxford University Press, New York, 2018).
[47] A. D. Ratschow, S. Stein, and H.-J. Gross, Process Safety Progress **42**, 362 (2022).
[48] N. Gibson and F. C. Lloyd, J. Phys. D **3**, 563 (1970).
[49] M. Zdanowski and M. Maleska, Arch. Electr. Eng. **68**, 387 (2019).
[50] M. Kaponig, A. Mölleken, H. Nienhaus, and R. Möller, Sci. Adv. **7**, eabg7595 (2021).
[51] E. Lauga, M. Brenner, and H. Stone, in *Springer Handbook of Experimental Fluid Mechanics*, edited by C. Tropea, A. L. Yarin, and J. F. Foss (Springer, Berlin, 2007), pp. 1219–1240.
[52] D. M. Huang, C. Sendner, D. Horinek, R. R. Netz, and L. Bocquet, Phys. Rev. Lett. **101**, 226101 (2008).
[53] P. A. Thompson and M. O. Robbins, Phys. Rev. Lett. **63**, 766 (1989).
[54] A. Dörr and S. Hardt, Phys. Fluids **26**, 082105 (2014).
[55] W. S. Y. Wong, P. Bista, X. Li, L. Veith, A. Sharifi-Aghili, S. A. L. Weber, and H.-J. Butt, Langmuir **38**, 6224 (2022).
[56] O. V. Voinov, Fluid Dyn. **11**, 714 (1977).
[57] R. G. Cox, J. Fluid Mech. **168**, 169 (1986).
[58] M. D. Morris and J. J. Lingane, J. Electroanal. Chem. (1959) **6**, 300 (1963).
[59] P. Vogel, N. Möller, M. N. Qaisrani, P. Bista, S. A. L. Weber, H.-J. Butt, B. Liebchen, M. Sulpizi, and T. Palberg, J. Am. Chem. Soc. **144**, 21080 (2022).
[60] B. J. Kirby and E. F. Hasselbrink, Electrophoresis **25**, 187 (2004).
[61] A. Alizadeh Pahlavan, L. Cueto-Felgueroso, G. H. McKinley, and R. Juanes, Phys. Rev. Lett. **115**, 034502 (2015).